Dual-Porosity Carbon Templated from Monosize Mesoporous Silica Nanoparticles

Jiawen Ren,[†] Jie Ding,[†] Kwong-Yu Chan,*[,†] and Huanting Wang[†,‡]

Department of Chemistry, The University of Hong Kong, Pokfulam Road, Hong Kong SAR, P. R. China, Department of Chemical Engineering, Monash University, Clayton, Victoria, 3800, Australia

Received September 11, 2006. Revised Manuscript Received March 9, 2007

A mesoporous carbon structure was template-synthesized from small nanoparticles of silica with internal M41S type mesopores. The silica template was synthesized according to Suzuki et al. using an ionic surfactant to create the internal mesopores 1.8−3.5 nm diameter and a nonionic surfactant to limit the overall size of the particle. Larger mesopores in the silica are needed for carbonization to a better structure. This was achieved by the use of a swelling agent, trimethylbenzene (TMB). Characterization by transmission electron microscopy (TEM), X-ray diffraction (XRD), and nitrogen sorption analysis showed a mesocellular foamlike carbon structure composed of porous cells with internal hexagonally arranged channels. In addition to the 3 nm internal channels, there were larger mesopores connecting the cellular domains. These larger mesopores were formed in the interparticle voids created during carbonization. The dual porosity network structure had a high surface area (>1000 m^2/g) and large pore volume (>1.2 mL/g). When loaded with Pt−Ru nanoparticles, the PtRu/carbon became a good electrocatalyst and gave the highest activity for methanol oxidation among several PtRu electrocatalysts including commercial electrocatalysts.

1. Introduction

Rapid advances have been made in the synthesis of porous carbon materials with controlled and tunable nanostructures.[1,2] These materials are investigated for applications as catalysts supports,[3−6] adsorbents,[7] and energy materials.[8−10] In addition to high surface area and high porosity, their well-defined structures serve as convenient materials for systematic fundamental studies in which structure−property relations are to be developed.[11] Mathematical modeling to study confined transport processes can be more readily implemented on these well-defined support structures compared to common high-surface-area carbons. The carbonization step to make the carbon structure is carried out at elevated temperatures and structure-directing agents would have been decomposed. Therefore, a popular synthetic route is to make the complementary structure out of a hard thermal stable nanoporous template material such as the well-known mesoporous silicas. Examples of these silicas with ordered mesopores are Mobil catalytic materials number 41 and 48 (MCM-41, MCM-48),[12,13] Santa Barbara amorphous number 15 (SBA-15)[14] and Fu-Dan University number 12 (FDU-12).[15] Variation of mesoporous structures with different pore sizes, surface area, pore volume, pore shapes, and spacing is achieved by the choice of the structure-directing agent and parameters in the synthetic steps.[16] The resulting template-synthesized carbon structures are the complementary geometries. The general synthetic route of these ordered mesoporous carbons (OMCs) was first reported by Ryoo and coworkers in 1999.[17] OMCs have highly ordered pore structures, high surface area, large pore volume, and pore sizes tunable by the appropriate choice of surfactant and synthesis parameters.[1,2]

One of the inherent problems in applying these OMC materials is the limited mass-transfer through the long and narrow channels.[18,19] As a result, the electrochemical activity

* To whom correspondence should be addressed. Phone: 852 28597917. Fax: 852 29155176. E-mail: hrsccky@hku.hk (K.-Y.C.).
[†] The University of Hong Kong.
[‡] Monash University.

(1) Lee, J.; Han, S.; Hyeon, T. *J. Mater. Chem.* **2004**, *14*, 478.
(2) Yang, H.; Zhao, D. *J. Mater. Chem.* **2005**, *15*, 1217.
(3) Joo, S. H.; Choi, S. J.; Oh, I.; Kwak, J.; Liu, Z.; Terassaki, O.; Ryoo, R. *Nature* **2001**, *412*, 169.
(4) Chan, K. Y.; Ding, J.; Ren, J.; Cheng, S.; Tsang, K. Y. *J. Mater. Chem.* **2004**, *14*, 505.
(5) Yu, J. S.; Kang, S.; Yoon, S. B.; Chai, G. *J. Am. Chem. Soc.* **2002**, *124*, 9382.
(6) Su, F.; Zeng, J.; Bao, X.; Yu, Y.; Lee, J. Y.; Zhao, X. S. *Chem. Mater.* **2005**, *17*, 3960.
(7) Lu, A.; Schmidt, W.; Matoussevitch, N.; Bönnemann, H.; Spliethoff, B.; Tesche B, Bill, E.; Kiefer, W.; Schüth, F. *Angew. Chem., Int. Ed.* **2004**, *43*, 4303.
(8) Lee, J.; Yoon, S.; Oh, S. M.; Shin, C. H.; Hyeon, T. *Adv. Mater.* **2000**, *12*, 359.
(9) Liu, H.; Wang, K.; Teng, H. *Carbon* **2005**, *43*, 559.
(10) VixGuterl, C.; Saadallah, S.; Jurewicz, K.; Frackwiak, E.; Reda, M.; Parmentier, J.; Patarin, J.; Beguin, F. *Mater. Sci. Eng., B* **2004**, *108*, 148.
(11) Solovyov, L. A.; Kim, T. W.; Kleitz, F.; Terasaki, O.; Ryoo, R. *Chem. Mater.* **2004**, *16*, 2274.
(12) Kresge, C. T.; Leonowicz, M. E.; Roth, W. J.; Vartuli, J. C.; Beck, J. S. *Nature* **1992**, *359*, 710.
(13) Beck, J. S.; Vartuli, J. C.; Roth, W. J.; Leonowicz, M. E.; Kresge, C. T.; Schmitt, K. D.; Chu, C. T. W.; Olson, D. H.; Sheppard, E. W.; McCullen, S. B.; Higgins, J. B.; Schlenker, J. L. *J. Am. Chem. Soc.* **1992**, *114*, 10834.
(14) Zhao, D.; Feng, J.; Huo, Q.; Melosh, N.; Fredrickson, G. H.; Chmelka, B. F.; Stucky, G. D. *Science* **1998**, *279*, 548.
(15) Fan, J.; Yu, C.; Gao, F.; Lei, J.; Tian, B.; Wang, L.; Luo, Q.; Tu, B.; Zhou, W.; Zhao, D. *Angew. Chem., Int. Ed.* **2003**, *42*, 3146.
(16) Zhao, D.; Huo, Q.; Feng, J.; Chmelka, B. F.; Stucky, G. D. *J. Am. Chem. Soc.* **1998**, *120*, 6024.
(17) Ryoo, R.; Joo, S. H.; Jun, S. *J. Phys. Chem. B* **1999**, *103*, 7743.

10.1021/cm0621545 CCC: $37.00
Published on Web 05/03/2007

of electrocatalysts made with these OMC supports, e.g., PtRu supported on carbon mesoporous from KAIST number 3 (CMK-3)[20] was not as high as anticipated, as observed in methanol oxidation,[19] despite their high surface area and large pore volume. The pore size of OMC appears to be optimum in the range of a few nanometers, considering the anchoring and dispersion of Pt−Ru nanoparticles. The lengths of the pores are, however, at least 2 orders of magnitude too large and are related to the overall size of the carbon particle. The size of the carbon particle is in turn affected by the size of the silica template, usually in the range of hundreds of nanometers to a few micrometerss.[21,22] In view of mass-transfer limitations, it is advantageous to control the particle size of the ordered mesoporous silica. Zhang et al.[23] reported a procedure to make SBA-15 silica particles with the mesopores running along the short axes of the particles with lengths of 200 nm. Another scheme for making smaller mesoporous silica particles less than 50 nm diameter was suggested by Suzuki et al.[24] In their synthesis, a mesoporous M41S structure and the particle size are controlled by using of two surfactants: a cationic surfactant CTAC that generates the internal mesopores and a nonionic tri-block copolymer F127 that controls the overall size of the particle.

In this paper, we report the synthesis of a mesoporous carbon structure using small mesoporous silicas particles as templates. The mesoporous silica are monosize nanoparticles synthesized using the two-surfactant technique described by Suzuki et al.[24] The resulting carbons were found to have a bimodal pore structure and were tested to give high activity when supporting Pt−Ru nanoparticles for methanol oxidation.

2. Experimental Section

2.1. Synthesis of Dual Porosity Carbon. Following the procedure of Suzuki et al. ,[24] we made mesoporous silica template nanoparticles as follows. Three grams (3 g) of cetyltrimethylammonium bromide (CTAB) was dissolved in 30 mL of 0.32 M hydrochloric acid with pH 0.2 at room temperature. Five milliliters (5 mL) of trimethylbenzene (TMB) was then added. When the solution turned from milky to clear, 2 g of the triblock polyethylene oxide polypropylene oxide copolymer, Pluronic F127 $EO_{106}PO_{70}$-EO_{106}, was added and completely dissolved. Tetraethoxysilicate (TEOS), 3.5 g, was then added under stirring for 24 h to form a gel, at which point 4 g of 28% w/w ammonia water was added. The gel was aged at room temperature for 24 h, followed by drying and calcination at 600 °C. As opposed to Suzuki et al. ,[24] TMB was added to increase the diameter of the internal pores of the resulting silica structure and was found to yield a carbon structure with better properties. For comparison, silica particles with and without the addition of TMB were made and denoted as silica T and silica S, respectively. The corresponding carbon structures are denoted as carbon T and carbon S.

The carbonization procedure followed those described previously in the literature.[7,25] Furfuryl alcohol (FA) dissolved in trimethylbenzene (TMB) (v:v = 1:3) was used as carbon precursor with oxalic acid added as a polymerization catalyst. The molar ratio of FA to oxalic acid was 100. The FA solution was infiltrated into silica T or silica S at room temperature under ultrasonic treatment for 1 h. The solid−liquid mixture was treated in air at 80 °C for 16 h and 150 °C for 3 h with a heating rate of 1 °C min^{-1}. The final carbonization step was carried out at 900 °C under an argon flow for 4 h. After cooling, HF was used to remove the silica template from the resulting solid.

The loading of platinum−ruthenium nanoparticles into the mesoporous carbon followed a previously described procedure.[19,26] One milliliter of H_2PtCl_6 solution in ethylene glycol (EG) solution (15.2 mg Pt/mL) and 1.7 mL of $RuCl_3$ solution in EG (4.7 mg Ru/mL) and 5 mL EG were mixed together. With the pH adjusted to 13 by adding NaOH solution in EG (0.5 M), the solution was heated at 160 °C for 3 h under N_2 flow for the metal reduction reaction to proceed. Next, 50 mg of carbon support (carbon T or carbon S) was added to adsorb the colloidal metallic nanoparticles at room temperature for 12 h. The final product had 30% (m/m) Pt and Ru on carbon. After centrifugation, the resulting sample was dried under a vacuum for 12 h.

2.2. Electrochemical Measurements. Steady-state polarization curves and other electrochemical analyses were obtained with an AutoLab model PGSTAT 30 potentiostat using a three-electrode cell with Pt foil as counter electrode and $Hg|HgSO_4$ as reference electrode in a 0.5 M H_2SO_4 and 0.5 M CH_3OH solution. The working electrode was prepared by dispensing a solution of the PtRu/carbon powder, 5% Nafion, and ethanol onto a 0.785 cm^2 gold electrode to achieve a controlled amount of electrocatalyst per unit area after drying at 60 °C for 2.5 h. In addition to the synthesized PtRu supported on mesoporous carbons, commercial electrocatalysts were tested. They included a 30% loading PtRu (1:1) from ElectroChem Corp. and a 20% loading PtRu (1:1) from E-Tek. The carbon supports of these commercial electrocatalysts are of the Vulcan 72 type.

2.3. Materials Characterization. Powder X-ray diffraction (XRD) patterns were obtained using Cu Kα source radiation at 40 kV from a Siemens D5000 instrument. Transmission electron microscopy (TEM) was conducted on a Philips TECNAI 20 electron microscope operated with an acceleration voltage of 200 kV. A typical TEM specimen was prepared by dispensing a drop of catalyst powder suspension in ethanol onto holey carbon mesh copper grids and dried under a vacuum. Nitrogen sorption isotherms were measured with a Micromeritics ASAP 2020 analyzer at 77 K. The pore size distribution was calculated by the BJH (Barrett−Joyner−Halenda) method on the basis of the analysis of adsorption branch of the isotherm. The pore volume was taken at single point of $p/p^0 = 0.985$. For t-plot determination of micropore volume, the Harkins−Jura equation was adopted. X-ray photoelectron spectra of supported PtRu were recorded on a PHI 5600 spectrometer (Physical Electronics) using an Al Kα source operating at 350 W.

3. Results

3.1. Structures of Silica Nanoparticles. The structures of the silica template nanoparticles were characterized by

(18) Xia, Y.; Mokaya, R. *Adv. Mater.* **2004**, *16*, 886.
(19) Ding, J.; Chan, K. Y.; Ren, J.; Xiao, F. *Electrochim. Acta* **2005**, *50*, 3131.
(20) Jun, S.; Joo, S. H.; Ryoo, R.; Kruk, M.; Taroniec, M.; Liu, Z.; Ohsura, T.; Terasaki O. *J. Am. Chem. Soc.* **2000**, 122, 10712.
(21) Yu, C.; Fan, J.; Tian, B.; Zhao, D.; Stucky, G. D. *Adv. Mater.* **2002**, *14*, 1742.
(22) Che, S.; Lund, K.; Tatsumi, T.; Ijima, S.; Joo, S. H.; Ryoo, R.; Terasaki, O. *Angew. Chem., Int. Ed.* **2003**, *42*, 2182.
(23) Zhang, H.; Sun, J.; Ma, D.; Bao, X.; Klein-Hoffmann, A.; Weinberg, G.; Su, D.; Schlögl, R. *J. Am. Chem. Soc.* **2004**, *126*, 7440.
(24) Suzuki, K.; Ikari, K.; Imai, H. *J. Am. Chem. Soc.* **2004**, *126*, 462.
(25) Lu, A.; Li, W. C.; Schmidt, W.; Kiefer, W.; Schüth, F. *Carbon* **2004**, *42*, 2939.
(26) Bock, C.; Paquet, C.; Couillard, M.; Botton, G. A.; MacDougall, B. R. *J. Am. Chem. Soc.* **2004**, *126*, 8028.

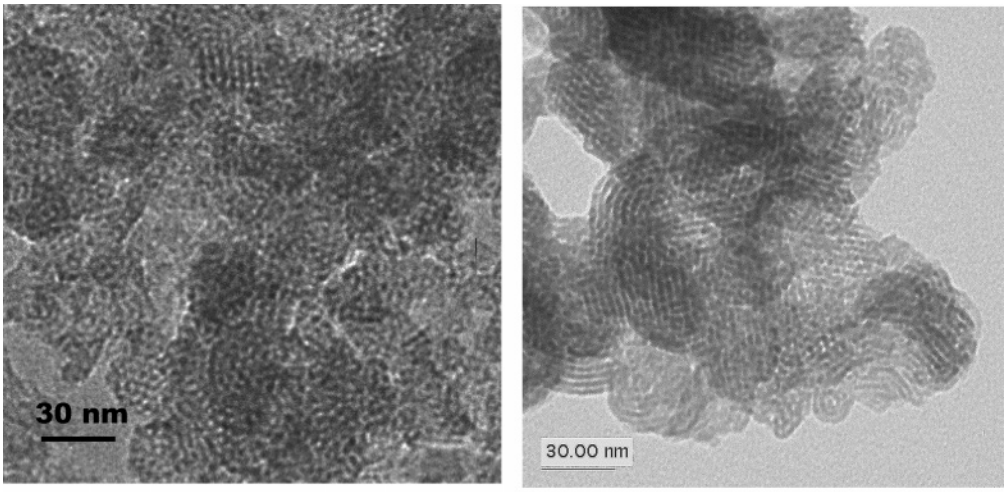

Figure 1. Transmission electron microscopy (TEM) images of (a) Silica S and (b) Silica T.

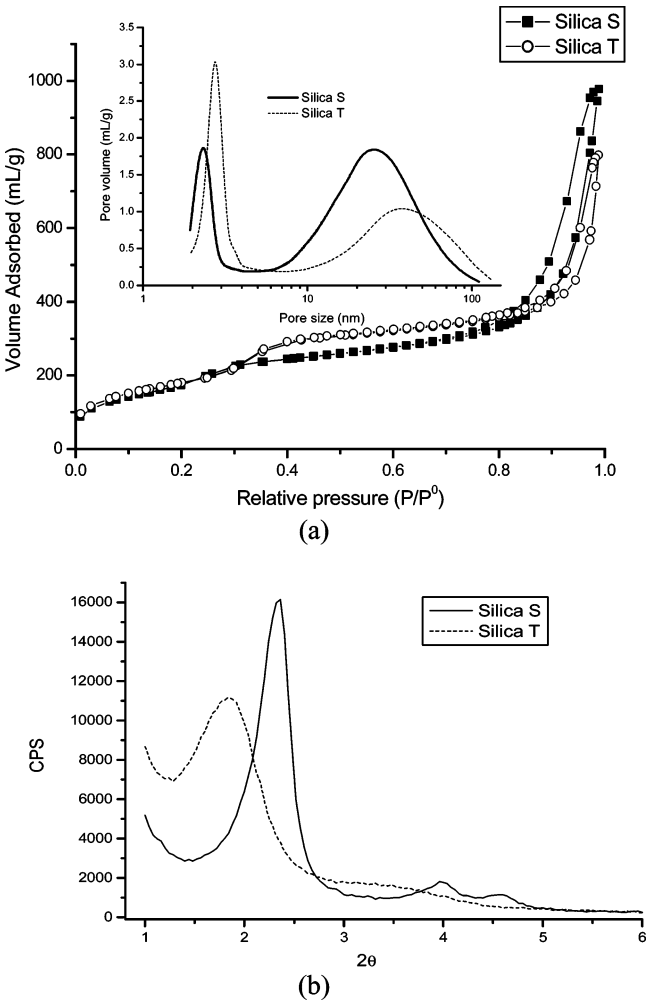

Figure 2. (a) Upper panel: nitrogen sorption isotherms of silica S and silica T and their pore size distributions in inset. (b) Lower panel: small-angle XRD patterns of silica S and silica T.

TEM, nitrogen sorption, and XRD. The characterization results are shown in Figures 1 and 2, and the corresponding structural parameters summarized in Table 1.

As shown in the TEM image of Figure 1a, the particle size of silica S was around 20 nm and the pores of a single particle were hexagonally arranged. From the nitrogen sorption isotherm shown in Figure 2a, silica S had a surface area of 639 m^2 g^{-1} and two main pore structures. The pore size distribution in the inset was analyzed by the adsorption branch, showing a first peak (mesopore I) at 2.3 nm and another broader peak (mesopore II) averaged at 25 nm. The smaller pores (mesopore I) were inside the silica nanoparticle and the size analyzed from adsorption isotherm was larger than the TEM image. The larger pores (mesopore II) were attributed to interparticle spaces among the nanoparticles.[21] The total pore volume was 1.24 mL g^{-1} and mainly contributed by mesopores. The hexagonal and ordered arrangement of mesopores I was evident from the (100), (110), and (200) peaks in the XRD spectrum of Figure 2b giving a spacing of 3.74 nm between the (100) lattice planes, consistent with a *p6mm*-type packing. All these structural results of silica S were consistent with those of Suzuki et al.[24] as compared in Table 1.

The addition of TMB in the synthesis gave observable changes to the structures, comparing the TEM images of Figure 1, nitrogen sorption isotherms of Figure 2a, and XRD patterns of Figure 2b for silica S and silica T. The size of the silica T particles and their mesopores appeared larger (Figure 1b). The pore size distribution from adsorption branch (inset of Figure 2a) shows larger mesopores I with a narrower peak at 2.9 nm and larger mesopores II with a peak at 36 nm. According to Suzuki et al.,[24] mesopore I was due to cylindrical micelles formed by the cationic surfactant and the role of F127 was to control the size of the nanoparticle. As expected, TMB acted as a swelling agent and would be solubilized within the cylindrical micelles, thus giving larger mesopores I.

A secondary effect of the TMB was a larger particle size caused by the larger cylindrical micelles. There could be changes in the free-energy balance between the surrounding non-ionic surfactant and the larger cylindrical micelles that have a smaller surface-charge density. Comparing TEM images a and b of of Figure 1, it was not apparent that there were more pores within a single nanoparticle of silica T. It was known in the literature that some order in the mesopore arrangement would be lost when a swelling agent was added.[13] The XRD spectra of Figure 2b confirmed that silica T was less-ordered, although the (100) peak was

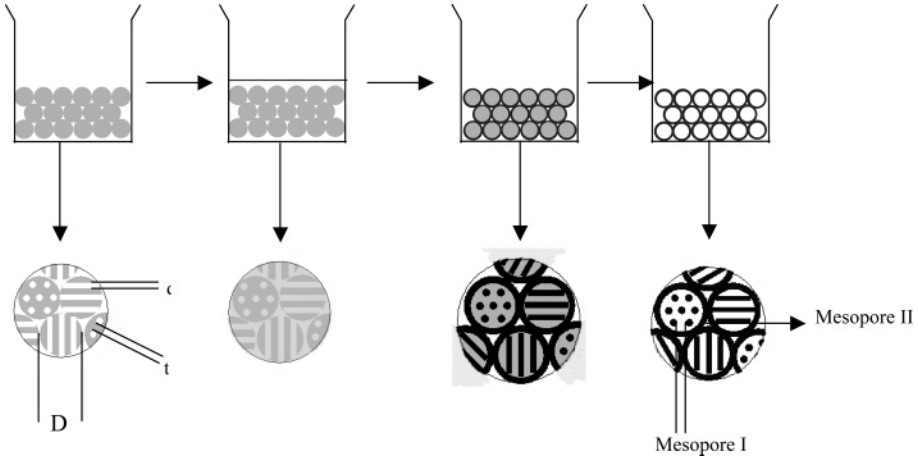

Figure 3. Schematic illustrations of synthesis of silica T (upper panel) and carbon T (lower panel).

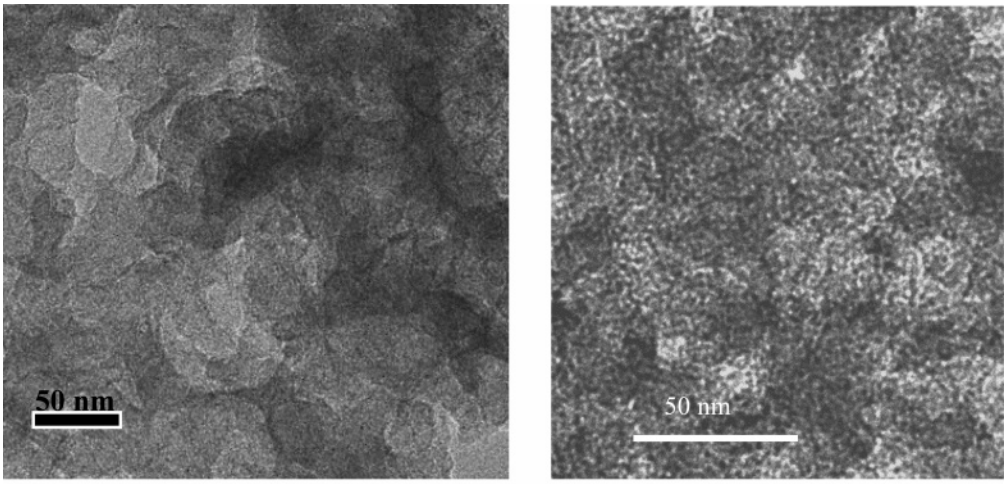

Figure 4. Transmission electron microscopy (TEM) images of (a) carbon S and (b) carbon T.

Table 1. Structural Parameters of Silica S and Silica T

samples	particle size (nm)	surface area (m^2/g)	t-plot micropore volume	total pore volume (mL/g)	d_{100} from XRD (nm)	cell param[a] a_o (nm)	pore size from TEM (nm)	wall thickness,[b] t (nm)	pore size from N_2 adsorption (nm)	interparticle mesopore size from N_2 adsorption (nm)
silica S	20−50	639	∼0	1.24	3.74	4.32	1.8	2.53	2.3	25
silica T	30−50	655	∼0	1.28	4.82	5.57	3.5	2.07	2.9	36
Suzuki et al.[24]	20−50				3.7	4.27			2.3	20

[a] Cell parameter a_o was calculated as $2d_{100}$ /Ö3. [b] Wall thickness was calculated by $t = a_o$ − pore diameter from TEM.

still observed with a corresponding lattice spacing of 4.82 nm. The structural data of silica T are also shown in Table 1. From the difference between the lattice spacing and size of mesopore I, the thickness of the silica wall can be estimated to be around 2.0 nm in both silica S and silica T.

3.2. Carbonization. Carbonization of silica S and silica T impregnated with carbon precursors formed carbon S and carbon T, as shown schematically in Figure 3. These carbon structures were characterized by TEM, nitrogen sorption, and XRD with results shown in Figures 4 and 5, respectively. The TEM images of the carbon structures in Figure 4 show a conglomerate of domains with uniformally sized mesopores. They resemble a mesocellular foam structure. The domains are not spherical but are uniformly sized, templated from the silica nanoparticles.

From the TEM images, the mesopores in carbon T appeared to be larger than carbon S. This is contrary to the pore size distributions shown in Figure 5, as analyzed from nitrogen sorption. The pore size distribution in carbon T in inset of Figure 5a shows two clear peaks at 3 and 13 nm, retaining the dual porosity nature of the template. The distribution of pore sizes in carbon S, however, was more spread out between 5 and 50 nm with an average about 18 nm. The surface area and pore volume of carbon T were 1043 $m^2\ g^{-1}$ and 1.22 mL g^{-1}, respectively. These are much higher than the values 620 $m^2\ g^{-1}$ and 0.87 mL g^{-1} of carbon S. The data of the two carbon structures are compared in Table 2 together with CMK-3 synthesized with the literature procedure.[20]

It is interesting to note that while silica S had a more ordered pore arrangement than silica T, the structure of

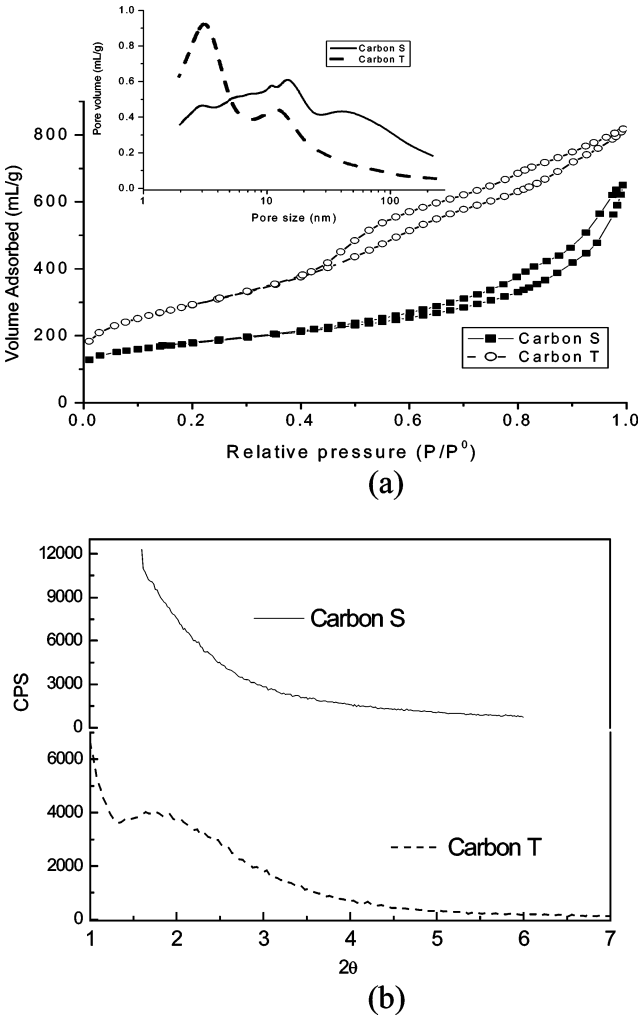

Figure 5. (a) Upper panel: nitrogen adsorption isotherms of carbon S and carbon T and their pore size distributions in inset. (b) Lower panel: small-angle diffraction pattern of carbon S and carbon T.

carbon T was more ordered, as shown in the XRD spectra of Figure 5b. A small (100) peak appeared in the XRD spectrum of carbon T, indicating a hexagonal arrangement of pores. Although the two silica templates S and T have similar structures and pore-distributions, the resulting carbon replicas have very different pore distributions. The role of TMB in making silica T is to enlarge the internal pores (mesopore I) and it is evident that sufficiently large mesopores are necessary to create the carbon replica. Earlier attempts to synthesize carbon replicas from M41S type meosporous silica had not been very successful because the complementary structure would be disconnected carbon rods.[8,27] The structures of carbon S and carbon T here should also be composed of carbon rods that came from filling the mesopores of the silica template. Because the silica nanoparticles were small, the carbon rods were of finite lengths and could be connected at the ends by a shell structure that formed round the silica particle. As shown in Figure 3, the carbon precursor liquid wetted the interparticle space of silica template nanoparticles, in addition to filling the internal mesopores. As carbonization proceeded, the liquid volume contracted, creating voids between the shell structures. These interparticle voids formed the larger mesopores (mesopore II) in the pore distribution. For carbon S with small mesopores I, smaller diameter carbon rods are formed and were not able to sustain the overall structure, yielding a broader size distribution of less-ordered pores. The size of mesopore I in carbon T, 3 nm, is close to the interchannel wall thickness of silica T, 2 nm, estimated from the size of mesopore I and d_{100} lattice spacing in Table 1. Normally, there is a shrinkage of nanorods during carbonization and silica removal. So the pore size in carbon T should be slightly larger than the silica wall thickness. From the value of the d_{100} spacing in carbon T and the size of mesopore I, the thickness of carbon wall between mesopores I would be 3.1 nm, again corresponding closely to the mesopore size of silica T. On the other hand, the size of mesopore II in carbon T was 13 nm, much smaller than the corresponding value of 30 nm in silica T. Mesopore II in silica T was due to interparticle space. This space would be filled up with the carbon precursor and the carbon formed subsequently. Mesopore II would therefore be the voids created during carbonization. These voids were the interstitial space between the spherical shells, as illustrated in Figure 3.

The overall particle size of carbon T or carbon S was large, as seen in Figure 4, and appeared to possess the same transport limitations as in CMK-3 with long and narrow channels. The orientations of mesopore I are hexagonally arranged but only over a small length scale of less than 30 nm. Beyond this length scale, the mesopores I are interconnected by larger channels of mesopores II, facilitating good transport. The dual porosity structure composed of small mesoporous domains networked by larger pores would therefore have good mass-transfer properties.

3.3. Support of PtRu Nanoparticles. The application of the novel mesoporous carbon structures as an electrocatalyst support was investigated by loading them with platinum ruthenium nanoparticles commonly used as anode catalyst of direct methanol fuel cells. The synthesized platinum−ruthenium nanoparticles supported on carbon S and carbon T were characterized by TEM and the images are shown in Figure 6. It can be observed that Pt−Ru nanoparticles were more uniformly dispersed in carbon T, whereas they were more connected in PtRu/Carbon S. The better dispersion could be due to the pore size distribution of carbon T having a well-defined peak at about 3 nm, which fit the size of the PtRu nanoparticles. From statistics of more than 300 particles in the TEM images, the PtRu particles size distribution was narrow and centered at 2.2 nm. The high-resolution transmission electron microscopy (HRTEM) image of PtRu/Carbon T in Figure 6c shows good crystallinity of the metal nanoparticles.

The XRD patterns of PtRu supported on various carbon supports are shown in Figure 7. The diffraction patterns of the different samples are similar with well-defined peaks corresponding to those of Pt(111), Pt(200), Pt(220), and Pt-(311) planes. The xrd patterns of carbon T and carbon S were obtained in a separate experiment from those of the commercial samples and hence their XRD intensities cannot

(27) Ryoo, R.; Joo, S. H.; Kruk, M.; Jaroniec, M. *Adv. Mater.* **2001**, *13*, 677.

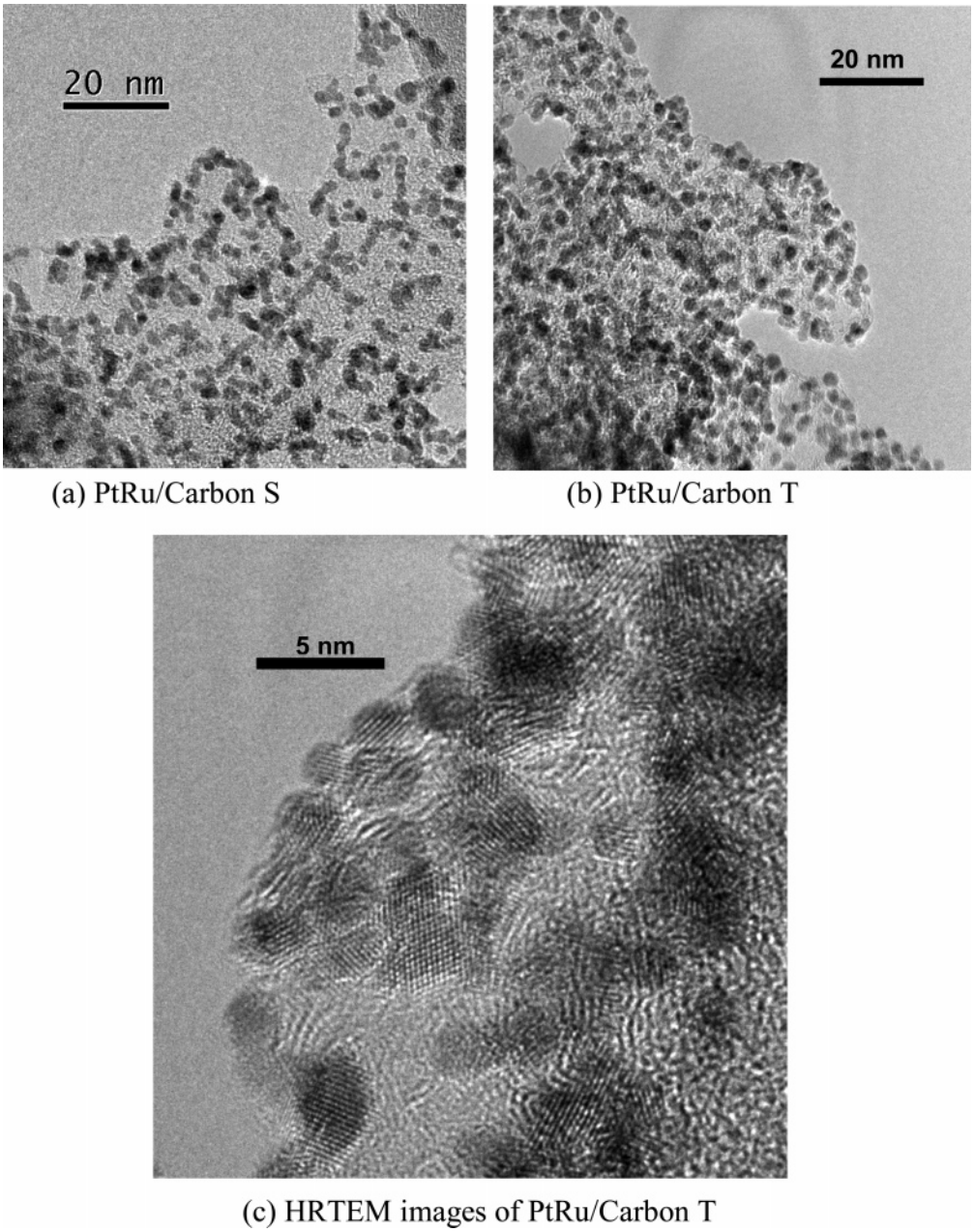

Figure 6. Transmission electron microscopy (TEM) images of (a) PtRu/carbon S, (b) PtRu/carbon T, and (c) PtRu/carbon T at high resolution (HRTEM)

Table 2. Structural Parameters of Carbon S, Carbon T, CMK-3, Vulcan-XC 72, and PtRu Loaded on Different Carbons

samples	surface area (m^2/g)	t-plot micropore volume	total pore volume (mL/g)	d_{100} from XRD (nm)	cell param (nm)	pore size from TEM (nm)	pore size from adsorption (nm)	interparticle pore size (nm)
Carbon S	620	0.1	0.87				multiple peaks and broad dist.	
Carbon T	1043	0.056	1.22	4.70	5.43	2.3	3	13
CMK-3	1026	0.102	1.237	7.36	8.49	6.0,[a] 2.8[b]	3.9	
Vulcan XC-72	201	0.039	0.383					
30%PtRu on Carbon T	452	~0	0.47					
20% PtRu on CMK-3	909	0.099	1.039					
ElectroChem (30%PtRu)	166	0.024	0.26					
ETeK (20%PtRu)	155	0.014	0.38					

[a] Diameter of carbon nanorods from TEM images. [b] Distance between carbon nanorods from TEM images.

be compared directly. From the broadening of the diffraction peaks, the mean size of the nanoparticles in carbon T was 2.3 nm, according to Scherrer's equation.[28] This number is consistent with the mean size of 2.2 nm observed from HRTEM. The Pt(111) peak in the PtRu electrocatalyst shifted to a higher 2θ value, compared to the pure Pt value of 39.8°. This suggests some alloying of the two metals and substitution of Pt by Ru in the Pt fcc lattice. From the shift of Pt-(111) peak, the cell lattice parameter was 0.2247 nm and a

(28) Cullity, B. D.; Stock, S. R. *Elements of X-ray Diffraction*, 3rd ed.; Prentice Hall: Upper Saddle River, NJ, 2001.

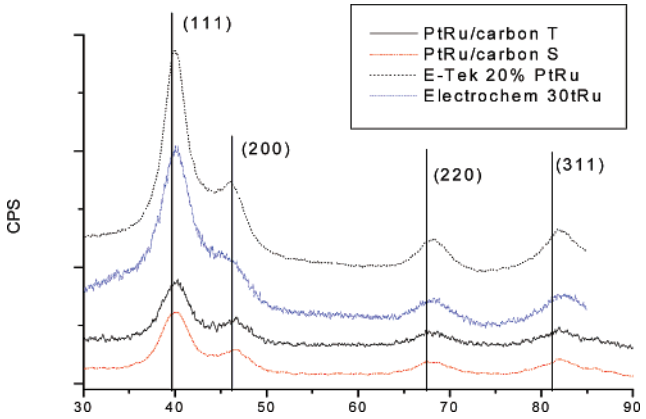

Figure 7. Powder XRD patterns of PtRu supported on various carbons.

Table 3. Binding Energies and Relative Intensities of Different Oxidation States of Pt and Ru in Carbon T and in ElectroChem Catalyst

catalyst	species	binding energy (eV)	relative intensity (%)
30% PtRu/carbon T	Pt(0)	71.25[a]	71.4
	Pt(II)	72.30[a]	28.6
	Ru(0)	462.1[b]	33.9
	RuO_2	463.6[b]	37.7
	$RuO_2{\cdot}xH_2O$	466.0[b]	29.4
30% PtRu/C (Electrochem)	Pt(0)	71.30[a]	75.8
	Pt(II)	72.50[a]	24.2
	Ru(0)	462.0[b]	42.9
	RuO_2	463.5[b]	44.3
	$RuO_2{\cdot}xH_2O$	466.1[b]	12.8

[a] Pt_{4f} peak position. [b] Ru_{3p} peak position.

Pt:Ru atomic ratio of 59:41 could be estimated according to Vegard's law.[29,30]

The results of energy dispersive X-ray analyses (EDX) indicated a total metal loading of 30% and a Pt:Ru ratio of 1:1, which is consistent with the XRD results. Because the PtRu nanoparticles in carbon T and the commercial catalyst were prepared via different synthetic routes, there could be variations in the oxidation states of Pt and Ru in the electrocatalysts. X-ray photoelectron spectroscopy (XPS) analyses were therefore performed for PtRu/carbon T and PtRu/ElectroChem to investigate the oxidation states of the metals. Because the Ru 3d peaks ($3d_{3/2}$ = 284.3 eV) overlapped the C 1s peak (1s = 284.5 eV), Ru 3p peaks were employed to analyze the oxidation states of Ru in catalysts. Figures 8 and 9 show, respectively, the Pt_{4f} and Ru_{3p} sections of the XPS spectra of the supported PtRu samples. The Pt 4f and Ru 3p peaks were deconvoluted using the software XPS-Peak to determine the proportions of metals in various oxidation states. The results are tabulated in Table 3 for the two PtRu/carbon samples showing similar ratios of Pt(0) to Pt(II) and Ru(0):Ru(IV). Platinum was mainly present in the zero oxidation state with less than 30% Pt(II), whereas there was a significant amount of Ru(IV). These results are similar to those of the previous analyses of PtRu nanoparticles supported on Vulcan-72 XC prepared, e.g., via the oil-in-water microemulsion route.[31] It is believed that the minor differences in the Ru(0):Ru(IV) ratio would not contribute to the differences in electrochemical activity of the PtRu/carbons samples.

As shown in Table 2, the loading of PtRu significantly reduced the surface area of the carbon support. For PtRu/carbon T, the surface area and pore volume were 452 $m^2\ g^{-1}$ and 0.47 mL g^{-1}, respectively, compared to 1043 $m^2\ g^{-1}$ and 1.22 mL g^{-1} of the bare carbon T support. These values of PtRu/carbon T, however, were comparable to the bare carbon S support, indicating the large difference in the two carbon structures. Considering the reduction of pore volume after loading of PtRu, a large part of it was attributable to an increase in mass due to metal content without an increase in porosity. For a 30% metal loading, the PtRu/carbon T material contains only 70% porous carbon and the overall pore volume is therefore 0.854 mL g^{-1}. This value is still above the measured value of 0.47 mL g^{-1}, suggesting that much of the porosity was blocked by the PtRu nanoparticles. It was likely that the smaller mesopores (I) were blocked by adsorbed PtRu nanoparticles, whereas the large mesopores (II) still provided transport of materials to the catalysts.

The electrochemical performance of the synthesized mesoporous carbon for methanol oxidation in sulfuric acid was shown in the steady-state polarization curves of Figure 10. Shown in Figure 10 for comparison are the performance of PtRu on other carbon supports including CMK-3, commercial catalysts from ElectroChem and ETeK. The potential values were converted to normal hydrogen potential (NHE) using the standard $Hg/HgSO_4$ reference electrode value of 0.64 V NHE. For the ETek and CMK-3 supported PtRu, the loading of precious metal was 20% instead of 30% for the other samples. Since the current density in Figure 10 is scaled to unit mass of precious metal (Pt and Ru), the comparison is still meaningful. On the basis on equal PtRu loading, a 100−300% increase in current density was observed on PtRu/carbon T compared to the commercial electrocatalysts.

It would be interesting to compare the performance of PtRu supported on carbon T and carbon S which are templated from a similar silica structure. The performance of PtRu/carbon T was better than PtRu/carbon S, probably due to larger surface area and porosity. However, it is the precious metal and not carbon that is playing the role of catalyst. The difference in electrochemical performance should be interpreted by the difference in the overall porous structure, because metal nanoparticles were synthesized in the same procedure, giving the same composition and loading.

Near open circuit potential and at low current densities, there was little or no difference in electrocatalytic performance of the different electrodes because the inherent kinetics and metal surface areas were similar. The difference in activity was mainly due to mass-transfer effects in the nanostructures and apparent only at higher currents. Carbon S showed disordered structure with large pore size and small pore volume. Carbon T had high surface area, large pore volume, and a clear bimodal pore distribution. After PtRu

(29) Bock, C.; MacDougall, B.; Lepage, Y. *J. Electrochem. Soc.* **2004**, *151*, A1269.
(30) Solla-Gullon, J.; Vidal-Iglesias, F. J.; Montiel, V.; Aldaz, A. *Electrochim. Acta* **2004**, *49*, 5079.
(31) Zhang, X.; Chan, K. Y. *Chem. Mater.* **2003**, *15*, 451.

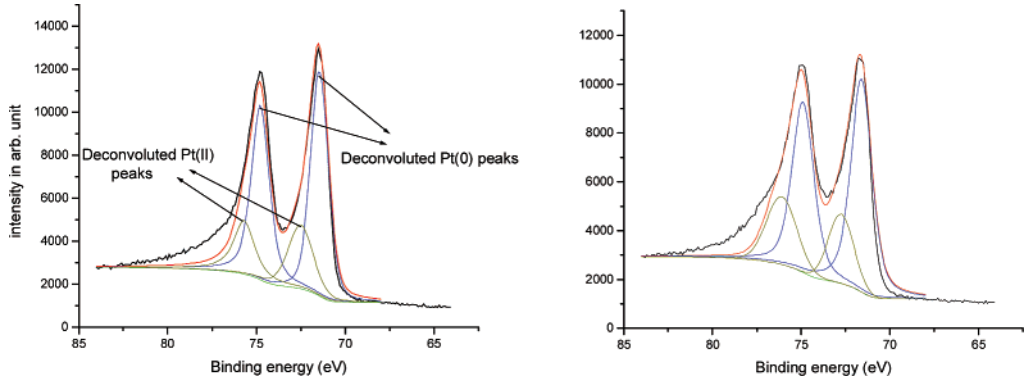

Figure 8. XPS spectra and deconvoluted curves for the Pt_{4f} region in PtRu/carbon T sample (left panel) and in PtRu/Electrochem (right panel).

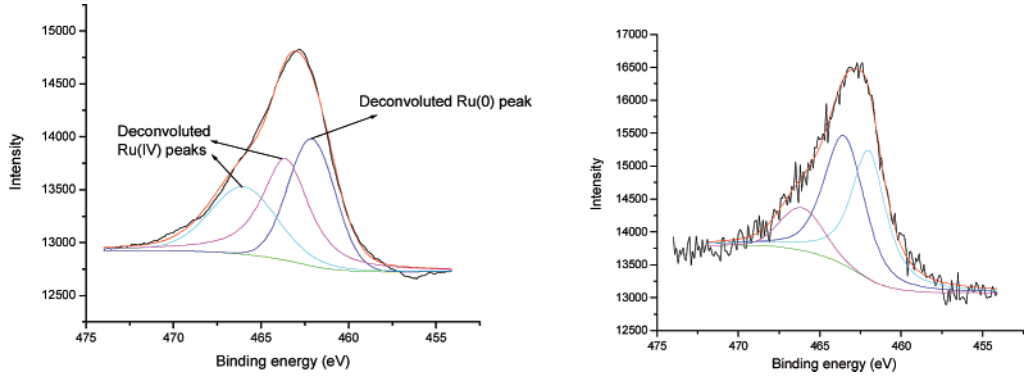

Figure 9. XPS spectra and simulated curves for the Ru_{3p} region in PtRu/carbon T sample (left panel) and in PtRu/Electrochem (right panel).

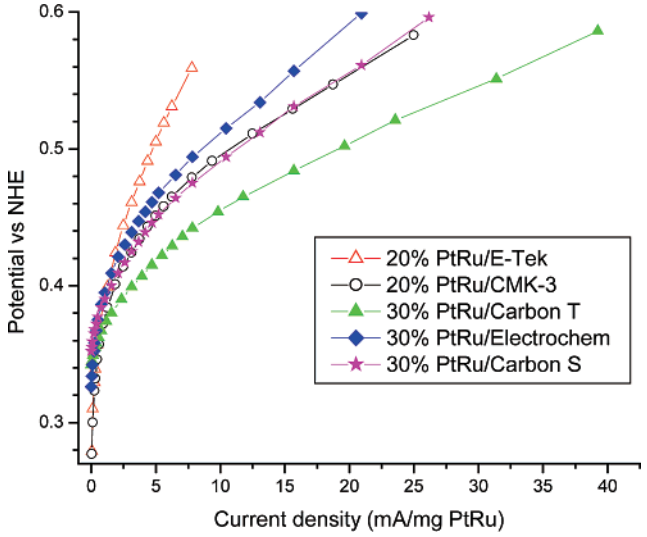

Figure 10. Polarization curves of methanol oxidation on PtRu supported by various carbon structures at room temperature.

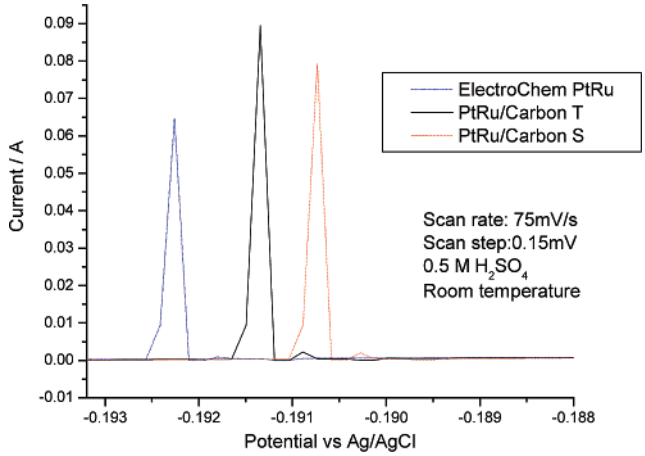

Figure 11. Hydrogen desorption peak in the anodic sweep of various PtRu/carbon electrodes precharged with hydrogen.

nanoparticles were loaded in carbon T, the surface area and pore volume of mesopores I drastically decreased, whereas pore size distribution and pore volume of micropores from t-plot did not change, indicating that nanoparticles were absorbed mainly in mesopores. This was also reasonable that ~2 nm colloidal PtRu particles cannot enter the micropores but resided in the mesopores in the carbon. The carbon with two sets of mesopores networked together appeared to be a favorable structure. The smaller mesopores act as adsorption sites for supporting the catalyst nanoparticles with good dispersion, while the large mesopores provide the channels for mass-transfer. Compared to PtRu/carbon T, PtRu/CMK-3 had a higher surface area and a pore volume. This was partially due to the lower metal loading and difference in their porous structures, but the performance of PtRu/CMK-3 on the basis of unit precious metal was inferior to that of PtRu/carbon T. This was probably due to the large particle size of CMK-3, rendering the interior of the long mesopores inaccessible particularly at high currents.

To investigate the relationship between parameters of the carbon structure and electrochemical performance, additional characterization experiments were performed. Hydrogen chemisorption is a standard method to estimate the surface area of platinum-ruthenium accessible to hydrogen. Chemisorption experiments, however, are conducted in a gaseous environment, whereas hydrogen or methanol in a fuel cell is in the dissolved state. A common alternative is to determine the electrochemical active area of precious metal via hydrogen desorption during a charging−discharging

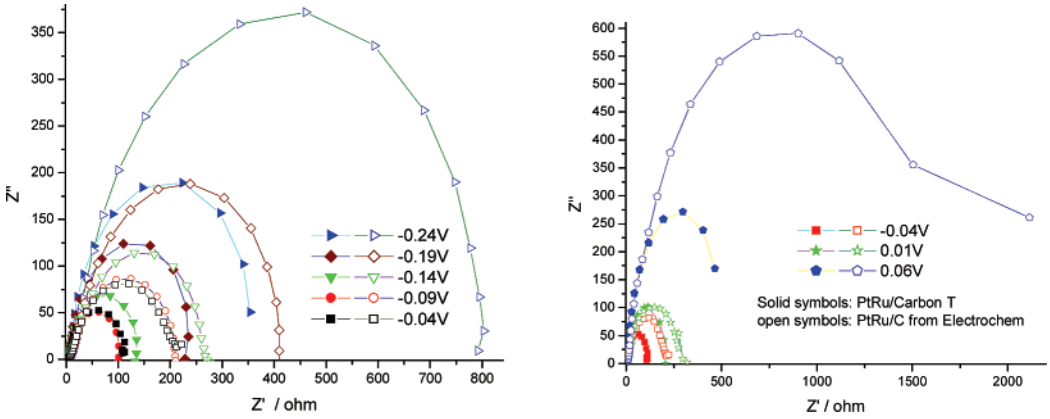

Figure 12. AC impedance plots of electrodes prepared with PtRu/carbon T (solid symbols) and PtRu/Electrochem (open symbols) at various potentials vs $Hg/HgSO_4$ in 0.5 MeOH and 0.5 H_2SO_4. (a) left panel: potentials below −0.04 V (b) right panel: potentials above −0.04V, scales of axes are different from those in left panel. (c) HRTEM images of PtRu/Carbon T.

electrochemical scan. Here, we modified the method of Ho and Piron[32] and performed a linear anodic sweep voltammetry experiment for a given PtRu/carbon sample in 0.5 M sulfuric acid to capture the hydrogen discharge wave, as shown in Figure 11.

The PtRu/carbon sample, 0.2 mg was coated onto a gold electrode as in the methanol oxidation experiment and kept a potential just positive to the hydrogen evolution potential for 180 s to charge the electrode with adsorbed hydrogen. A linear anodic sweep over a small window of 0.15 mV was then applied immediately to allow the adsorbed hydrogen to desorb with a simultaneous discharge current. The corresponding voltammograms are shown in Figure 11 for the three test samples. Double layer effects were negligible for such a small voltage range and the desorption peaks were distinct. Control experiments were performed for gold electrodes and gold electrodes with Nafion but without PtRu/carbon, showing no desorption peaks at all. The areas under the desorption peaks correspond to effective metal areas and are 222, 196, and 178 μC for PtRu supported on carbon T, carbon S, and the commercial Electrochem carbon, respectively. These results indicate that the electrochemical accessible area of the precious metal for the various samples follow the order of the performance in methanol oxidation. These values are electrochemically more relevant than the chemisorption surface areas as determined in a gaseous environment.

To further investigate the mass-transfer resistance in the porous network of a given PtRu/carbon sample, we conducted AC impedance experiments to determine the magnitude mass-transfer resistance and its correlation to the network porous structure. The experiments were conducted for the methanol oxidation reaction in 0.5 M sulfuric acid in the potential range of −0.24 to 0.06 V vs $Hg/HgSO_4$. The results of two samples PtRu supported on carbon T and on Electrochem carbon are shown in Figure 12.

These Cole−Cole impedance plots are in complex domains with the *x*-axis representing the real part components of impedance (resistance) with the high-frequency limiting impedance toward the origin. In the left panel for potentials between −0.24 and −0.04 V vs $Hg/HgSO_4$, impedance decreases with potential, corresponding to the first steps of the methanol reaction mechanism with C−H bond cleavage. In the right panel of Figure 12, for potentials above −0.04 V vs $Hg/HgSO_4$, impedance increases with potential probably because of a change in the mechanism with oxidation of CO to CO_2. These later reactions at high potential appeared to have more mass-transfer resistance. In all cases, the PtRu on carbon T showed lower impedance than PtRu on Electrochem carbon at the same frequency and same potential. This difference is more evident at high potentials, e.g., at 0.06 V when the impedance in PtRu on Electrochem carbon is 100% larger. The results indicated the importance of the porous structure to provide channels for mass-transfer in the methanol oxidation reaction. The AC impedance results at high potentials are therefore consistent with the steady-state polarization curves in Figure 10.

From the electrochemical studies, it can be observed that the accessible precious metal area play an important role for methanol oxidation at low overpotentials when the C−H bond cleavage reaction occurs. At high overpotentials, further oxidation of intermediates, e.g., CO is more limiting and efficient mass transport in the porous channels become more critical. The dual porosity carbon offers a favorably mesoporous structure with about 25% higher accessible precious metal area and >100% lower impedance at high overpotentials, compared to commercial electrocatalyst. The characterization resultsof porous structures presented here are by no means exhaustive. Recently, the xenon[129] NMR technique has been applied to probe the porous structure mesoporous materials where the xenon can be present in a dissolved state.[33,34] This technique can also be applied to probe metal surfaces[35] and is therefore very useful for studying PtRu adsorbed in mesoporous carbon and functioning as an electrocatalyst in an aqueous solution.

4. Conclusions

With the addition of a "swelling agent", the Suzuki method of double surfactant system could be modified to synthesize

(32) Ho, J. C. K.; Piron, D. L. *J. Electrochem. Soc.* **1995**, *142*, 1145.

(33) Zhang, W.; Han, X.; Liu, X.; Lei, H.; Bao, X. *Chem. Commun*. **2001**, 293.

(34) Telkki, V. V.; Lounila, J.; Jokisaari, J. *J. Phys. Chem. B* **2005**, *109*, 24343.

(35) Jansch, H. I.; Gerhard P.; Koch, M. *Proc. Natl. Acad. Sci., U.S.A.* **2004**, *101*, 13715.

M41S type mesoporous silica nanoparticles with sufficiently large mesopores for subsequent template-synthesis of mesoporous carbon. The resulting carbon structure resembles that of a mesocellular structure but the connected domains have hexagonally arranged mesopores with orientations randomly correlated to neighboring cells. These carbon structures exhibited high surface area and large pore volume and are potential catalysts supports. With PtRu nanoparticles supported on the carbon, the electrochemical activity for methanol oxidation was significantly higher than that of a commercial catalyst. High surface area, good dispersion, and adsorption of PtRu nanoparticles are provided by a set of small mesopores, whereas the large mesopores connecting them provide efficient mass transfer of ions and molecules.

Acknowledgment. This work is supported by the Research Grants Council of Hong Kong (HKU 7072/01P, HKU 7005/03P), a Joint Sino-German Collaborative Research Grant on "Fundamental Aspects of Direct-Alcohol Fuel Cells", and a seed grant from the HKU Foundation.

CM0621545